Journal of Thermal Analysis and Calorimetry (2020) 141:1801–1816
https://doi.org/10.1007/s10973-020-09658-z

Natural convection of nanoencapsulated phase change suspensions inside a local thermal non-equilibrium porous annulus

Farooq H. Ali[1] · Hameed K. Hamzah[1] · Masoud Mozaffari[2] · S. A. M. Mehryan[3] · Mohammad Ghalambaz[4,5]

Received: 5 January 2020 / Accepted: 31 March 2020 / Published online: 17 April 2020

Abstract

In this study, the heat transfer, fluid flow and heat capacity ratio are analyzed in an annulus enclosure filled with porous and saturated by a suspension of nanoencapsulated phase change materials (NEPCMs). It consists of phase change material core and a polymer or non-polymer shell. The presence of nanoparticles in the base fluid and the phase change capability of the nanoparticle's core improve the thermal properties of the base fluid and thermal control process. The inner cylinder wall is reserved at hot temperatures where the encapsulated particles absorb the heat, while the outer cylinder wall is reserved at cold temperatures where the encapsulated particles release the heat. A local thermal non-equilibrium model is adopted for the porous medium. The parameters studied are Rayleigh number ($10^4 \le Ra \le 10^6$), Stefan number ($0.2 \le Ste \le \infty$), melting point temperature of the core ($0.05 \le \theta_f \le 1$), the concentration of the NEPCM particles ($0\% \le \phi \le 5\%$), radius ratio ($1.67 \le Rr \le 2.5$), eccentricity ($-0.67 \le Ec \le 0.67$), Darcy number ($10^{-4} \le Da \le 10^{-1}$), porosity ($0.3 \le \varepsilon \le 0.9$) and interface heat transfer coefficient ($1 \le H \le 1000$). The results show that the dimensionless temperature of fusion (θ_f) plays the main role in the improvement in NEPCM on the heat transfer process.

Keywords Nanoencapsulated phase change materials (NEPCMs) · NEPCM suspension · Local thermal non-equilibrium (LTNE) · Heat transfer enhancement

✉ Mohammad Ghalambaz
mohammad.ghalambaz@tdtu.edu.vn

Farooq H. Ali
farooq_hassan77@yahoo.com

Hameed K. Hamzah
Hameedkadhem1977@gmail.com

Masoud Mozaffari
masoodmozafari66@yahoo.com

S. A. M. Mehryan
alal171366244@gmail.com

[1] Mechanical Engineering Department, College of Engineering, University of Babylon, Babylon, Iraq

[2] Department of Mechanical Engineering, Najafabad Branch, Islamic Azad University, Najafabad, Iran

[3] Young Researchers and Elite Club, Yasooj Branch, Islamic Azad University, Yasooj, Iran

[4] Metamaterials for Mechanical, Biomechanical and Multiphysical Applications Research Group, Ton Duc Thang University, Ho Chi Minh City, Vietnam

[5] Faculty of Applied Sciences, Ton Duc Thang University, Ho Chi Minh City, Vietnam

List of symbols

C_p	Specific heating for pressure constant (KJ kg^{-1} K^{-1})
Cr	Ratio of heat capacity of the suspension to base fluid
Da	Darcy number
f	Dimensionless form of phase change behavior
Ec	Eccentricity
g	Gravitational acceleration (m s^{-2})
h_{sf}	Latent heat of the core (kJ kg^{-1})
i	Number of grid case
k	Thermal conductivity (W m^{-1} K^{-1})
K	Permeability of the porous medium (m^2)
N	Mesh size
Nc	Suspension conductivity number
Nu	Nusselt number
Nv	Suspension dynamic viscosity
Pr	Prandtl number
Q_t	Total heat transfer rate
Rr	Radius ratio
r	Radius (m)
Ra	Rayleigh number
Ste	Stefan number
T	Temperature (K)
T_{Mr}	Temperature melting range (K)

u Velocity component in x-direction (m s^{-1})
U Dimensionless velocity component in X-direction
v Velocity component in y-direction (m s^{-1})
V Dimensionless velocity component in Y-direction
X, Y Dimensionless coordinate
ι Ratio of the mass of the NEPCM to the shell

Greek symbols

μ Fluid dynamic viscosity (kg s m^{-1})
α Thermal diffusivity (m^2 s^{-1})
β Thermal expansion coefficient (K^{-1})
Δ Dimensionless band of phase change
ε Porosity of the porous medium
θ Dimensionless temperature
λ Dimensionless heat capacity
ρ Density (kg m^{-3})
ϕ Nanoparticle volume fraction
ψ Dimensional stream function (m^2 s^{-1})
Ψ Dimensionless stream function
p Pressure of suspension (Pa)
P Dimensionless pressure of suspension
ν Kinematic viscosity (Pa s)

Subscripts

b NEPCM suspension
c Cold
co NEPCM core
bf Base fluid
f Fusion property
h Hot wall
i Inner
m Porous medium
p NEPCM nanoparticle
o Outer
s Solid matrix of the porous medium
sh NEPCM shell

Introduction

In engineering applications, natural convection is generally visualized in the development of cooling structures for electronics cooling, building conditioning, heat exchanger, molten material, solar collectors, nuclear reactors and devices for energy storage. The natural convection flows do not require a fan or moving components to circulate the flow. Hence, the maintenance cost, noise and failure of this type of heat transfer systems are low. The natural convection heat transfer is of interest in many engineering applications with the requirement of low-noise operation or involved safety issues. The disadvantage of natural convection heat transfer is the low cooling power compared to mixed or forced convection flow. Hence, any approach which could passively improve the natural convection heat is of great interest. Fluid consolidation by nanoparticles is one of the techniques to enhance the heat transfer rate with the increase in the thermal conductivity [1–3].

At the turn of the century, nanofluid has found a broad area of applications in natural convection phenomenon. Many researchers have been interested in studying the natural convection in different geometries and different types of nanofluids; for example, Khanafer and Vafai [4] studied natural convection inside square geometry enclosure using Cu–water nanofluid. The authors found a new correlation related between average Nusselt number with Grashof number and percentage volume fraction. The results show that increasing volume fraction percentage of nanoparticles improves heat transfer significantly. Jou and Tzeng [5] examined the natural convection in a rectangular enclosure shape filled with Cu–water nanofluid for various Rayleigh numbers and aspect ratios. An empirical correlation between the average Nusselt number and percentage of volume fraction was found. Sheikholeslami et al. [6] analyzed natural convection in the space between the inner hot sinusoidal cylinder and outer cold circular cylinder geometries under the effect of horizontal magnetic force suspended by Cu–water nanofluid. It is found that heat transfer rate increases with an increasing percentage of volume fraction of nanofluid, Rayleigh number and the number of corrugations, but decreases with the appearance and increasing Hartmann number. Ali [7] studied natural convection inside parallelogram enclosure geometry with Ag–water nanofluid. The researcher has found that the rate of heat transfer increases by increasing or decreasing the inclination angle from zero. Wang et al. [8] examined natural convection in a square cavity partially heated by the left wall and cooled by the right sidewall. Al_2O_3 nanoparticles with water as a base fluid filled the cavity. It is noticed that the effect of nanoparticles on the improvement in heat transfer increases with increasing Rayleigh number and volume fraction percentage, while heat transfer and average Nusselt number increase with decreasing length of the heater. At the end of this paragraph, it is worth noting that all the studies deal with nanofluid only.

Bhattacharya et al. [9] performed an analytical and experimental study on the thermophysical properties of metal foams with high porosity. Their research was classified into two parts of examining the thermal conductivity of the metal foam and then the permeability and inertial coefficients.

Moreover, outstanding review paper in applications of phase change material in energy storage is represented in [10, 11]. Wu et al. [12] investigated natural convection with heat generation inside a square porous cavity with constant non-equal and sinusoidal temperature of vertical walls, respectively. Leong and Lai [13] studied natural convection in porous annulus space with numerical transient and analytical Fourier transform solutions. The annulus space was filled with a sleeve layer of a porous medium. Using a

layer of the porous medium filled with liquids can improve the heat transfer. Using layers of porous medium or clear flow later was merged with nanofluid and studied by many researchers. In this regard, various aspects of the natural convection heat transfer are investigated for multilayer mediums [14], unsteady-state heat transfer in porous–nanofluid square enclosure [15], unsteady-state square enclosure occupied by porous–nanofluid and centered conductive square object [16], conjugate heat transfer [17], conjugate heat transfer with internal heat generation [18] and inclined cavity partially filled with a porous medium [19]. Chamkha et al. [20] and Ismael and Chamkha [21] addressed the natural convection of nanofluids in cavities filled with nanofluid or nanofluid and porous medium.

The local thermal non-equilibrium (LTNE) effects are significant when there is a notable temperature difference between the porous matrix and the host fluid. In such cases, the temperature of the host fluid and porous matrix can be represented using two different temperature fields. The LTNE has been investigated for nanofluid by some of the recent researchers [12, 15, 17, 18].

Now, phase change materials (PCMs) have been used in many industrial applications such as cooling and heating processes, power generation, production of food and pharmaceutical [22]. Fang et al. [23] used a nanoencapsulated phase change materials (NEPCMs) using core and shell techniques, urea and formaldehyde as a shell and *n*-tetradecane as the core. Qiu et al. [24] synthesized nanoencapsulated NEPCMs with the core containing *n*-octadecane, and a shell is made of a polymer methyl, methacrylate (MMA). Useful literature surveys were performed by Jamekhorshid et al. [25] and Su et al. [26] on the enhanced heat transfer in PCMs. Liu [27] studied the formation, description and applications of NEPCMs. Wickramaratne et al. [28] produced PCMs capsulated by low-cost ceramic materials having a melting temperature higher than 650 °C. Barlak et al. [29] conducted experimental studies of thermal conductivity and viscosity of nanofluids and nanoencapsulated phase change material. The results show that thermal conductivity and viscosity have opposite behaviors as the temperature increase. Zhu et al. [30] investigated an organic–inorganic hybrid NEPCMs with polymer–SiO_2 hybrid as a shell. This hybrid shell improves thermal properties such as conductivity, reliability and leakage proof.

The literature review shows that there are only a few studies on NEPCMs involving free convection heat transfer. Ghalambaz et al. [31] studied the nature of the square enclosure filled with a suspension of NEPCM particles and a host fluid. In another study, Ghalambaz et al. [32] addressed the mixed convection boundary layer heat transfer over a vertical flat plate. The results show that the fusion temperature is the main effecting factor on the enhanced heat transfer rate. Hajjar et al. [33] explored the unsteady natural convection behavior of NEPCMs in a cavity with a time-dependent wall temperature. The outcomes show that the fusion temperature of nanoparticle's notability affects the heat transfer in the enclosure. Dispersing 5% NEPCMs promotes the average Nusselt number from 9.19 (pure fluid) to 15.15 (NEPCM hybrid nanofluid), which is about 65% enhancement compared to the pure base fluid. In a very recent study, Ghalambaz et al. [34] investigated the unsteady natural convection of NEPCM suspensions in a porous enclosure, using a simple local thermal equilibrium (LTE) model of porous media. They assumed that the temperature of the porous matrix and the NEPCM suspension are identical. The results show that there is an optimal range of fusion temperature for heat transfer enhancement. The fusion temperature close to the average temperature of hot and cold isothermal walls is of practical heat transfer enhancement. Moreover, the thermal performance of NEPCM suspensions is substantial in porous media with high porosities.

Oztop and Abu-Nada [35] studied natural convection numerically in rectangular enclosure partially heated from the left wall. The authors used three types of nanoparticles (Cu, Al_2O_3 and TiO_2) with water as a working fluid. It is obtained that using nanofluid affects the fluid structure, temperature distribution and enhancement heat transfer rate. Varol et al. [36] carried out numerical study for entropy generation of conjugate free convection inside a trapezoidal cavity of right inclination wall superposed by a porous medium. The results show that the thermal conductivity ratio and layer thickness of the solid are the main important parameters, influencing the fluid pattern and the rate of heat transfer. Astanina et al. [37] analyzed the entropy generation due to unsteady natural convection inside an open trapezoidal enclosure filled with porous layer and ferro-nanofluid layer under the effect of inclination magnetic strength. It is found that the amplitude of average Nusselt number and average entropy generation increased with increasing Hartmann number.

Arshad et al. [38] carried out experimental study attention on cooling electronic equipment's utilizing heat sink system of pin–fin configuration superposed by PCM of different volume fractions. Qureshiet al. [11] made a review study on the enhancement thermal conductivity of PCM. The study was interested in the four ways that improved PCM thermal conductivity, using metallic nanoparticles having high thermal conductivity, using foam, using graphite and using encapsulation technique which has high thermal conductivity enhancement. Ali et al. [39] conducted an experimental study of pin–fin heat sink system having three types of pin–fin cross-sectional area (circular, rectangular and triangular) occupied 9% of volumetric space and immersed in PCM occupied 99% of volumetric space; six types of phase change material were examined to study its performance. Ali et al. [40] made a comparison of two shapes of pin–fin heat

sink systems: circular and square cross-sectional shape surrounded by PCMs (paraffin and *n*-eicosane). Rehman et al. [41] reported an experimental work of heat sink filled by copper foam and another type of heat sink filled by copper foam–PCM to notice the action of operative time of the system with detail to the sensors of temperature for cooling and heating process. Shah et al. [42] conducted a concisely study of the performance using hybrid nanofluid in solar energy. It is found that using hybrid nanofluid improved friction factor and pumping power. Abbas et al. [43] exhibit a significant revision of the action of nanoparticle execution improvement in PV-T regulation. The work grants a recent study of using nanoparticles to increase efficiency for PV and PV-T systems. Hassan et al. [44] performed experimental work on using nanofluid in PV-T and phase change material. Also, the researcher compared the results with PV system. The results show that utilizing nanofluid with phase change material gives improved performance than utilizing water phase change material system and phase change material alone.

The literature review shows that the NEPCM suspensions are a new type of energy storage media with a high capability of thermal energy storage and flexibility of heat transfer. However, there are only a few studies regarding the thermal modeling and heat transfer analysis of NEPCM suspensions. The metal foams are a promising medium for the application of NEPCM suspension during the charging and discharging process because of the high surface area of pores and notable interaction between the pores and NEPCM suspension.

Due to the high thermal conductivity of metal foams, the temperature of the porous medium and the working fluid could be much different. Thus, the local thermal non-equilibrium models are required to model the heat transfer in metal foams. As mentioned, Ghalambaz et al. [34] investigated the thermal behavior of NEPCM suspensions, employing a local thermal equilibrium model of a porous medium. Hence, following [34], the present work is the first attempt to study the thermal behavior of NEPCM suspensions using a local thermal non-equilibrium model (LTNE) by taking into account the temperature difference between the porous matrix and NEPCM suspension.

Problem physics

The considered geometry is a porous annulus of horizontal cylinders with the inner and outer radii of r_i and r_o, respectively. The ratio of the outer radius to the inner radius is Rr. As indicated in Fig. 1, the inner cylinder, located at (0, e), is heated at the temperature of T_h above the temperature of T_c of the outer cylinder. The pores of the porous annulus are occupied with a mixture of NEPCM particles and a host fluid. The shell and core of the NEPCM particles are, respectively, polyurethane (PU) and nonadecane, and water is considered the host fluid. Also, the solid matrix of the porous medium is made of glass balls. Figure 1 also demonstrates the different modes of the NEPCM particles while moving toward the cold and hot cylinders. The temperatures of the suspension and the solid matrix are locally different. In other words, a microscopic heat transfer establishes the energy balancing between the components of the porous medium. The thermophysical properties of the solid matrix, as well as the properties of the mixture components, are tabulated in Table 1. The melting

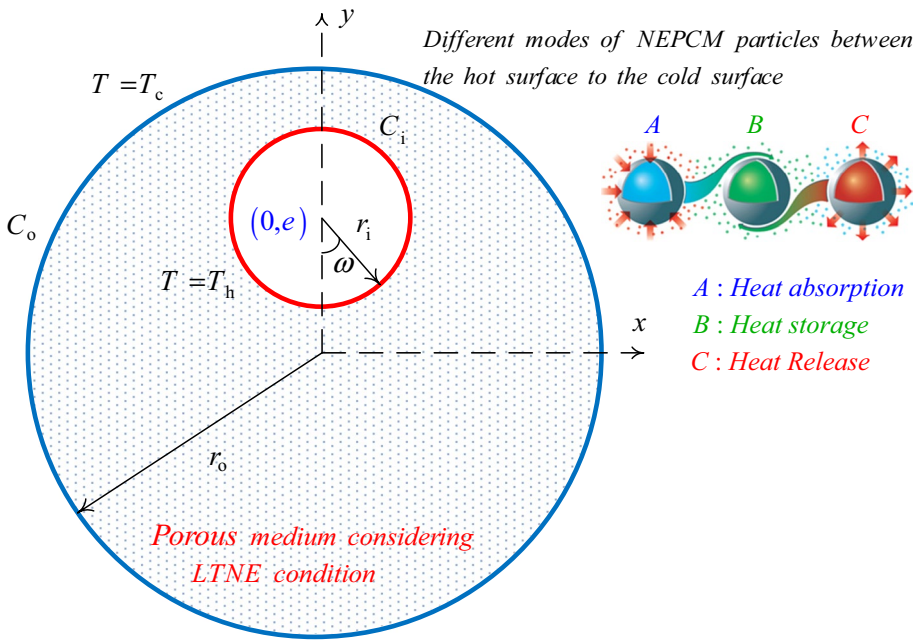

Fig. 1 Schematic configuration of the geometry as well as the different modes of the NEPCM particles

point temperature and latent heat of the nonadecane are about 32 °C and 211 kJ kg^{-1} [29].

The range of temperature variation for the nanofluids, which consist of a host liquid and nanoparticles, is quite low. In the case of nanoencapsulated phase change materials, the phase change occurs at a limited temperature band. Hence, the temperature variations in the cavity are limited, and the Boussinesq model is utilized in the present study.

Modeling approach

Applying the Boussinesq approximation to an incompressible, steady and Newtonian fluid flow, the equations describing the thermal and hydrodynamic characteristics of the water–NEPCM particle mixture flowing in a porous medium are

$$\frac{\partial u}{\partial x}+\frac{\partial v}{\partial y}=0 \tag{1}$$

$$\frac{\rho_{\mathrm{nf}}}{\varepsilon^2}\left(u\frac{\partial u}{\partial x}+v\frac{\partial u}{\partial y}\right)=-\frac{\partial p}{\partial x}+\frac{\mu_{\mathrm{nf}}}{\varepsilon}\left(\frac{\partial^2 u}{\partial x^2}+\frac{\partial^2 u}{\partial y^2}\right)-\frac{\mu_{\mathrm{nf}}}{\kappa}u \tag{2}$$

$$\frac{\rho_{\mathrm{nf}}}{\varepsilon^2}\left(u\frac{\partial v}{\partial x}+v\frac{\partial v}{\partial y}\right)=-\frac{\partial p}{\partial y}+\frac{\mu_{\mathrm{nf}}}{\varepsilon}\left(\frac{\partial^2 v}{\partial x^2}+\frac{\partial^2 v}{\partial y^2}\right)+g\rho_{\mathrm{nf}}\beta_{\mathrm{nf}}\left(T_{\mathrm{nf}}-T_{\mathrm{c}}\right)-\frac{\mu_{\mathrm{nf}}}{\kappa}v \tag{3}$$

$$\left(\rho C_{\mathrm{p}}\right)_{\mathrm{nf}}\left(u\frac{\partial T_{\mathrm{nf}}}{\partial x}+v\frac{\partial T_{\mathrm{nf}}}{\partial y}\right)=\varepsilon k_{\mathrm{nf}}\left(\frac{\partial^2 T_{\mathrm{nf}}}{\partial x^2}+\frac{\partial^2 T_{\mathrm{nf}}}{\partial y^2}\right)+h\left(T_{\mathrm{s}}-T_{\mathrm{nf}}\right) \tag{4}$$

$$0=(1-\varepsilon)k_{\mathrm{s}}\left(\frac{\partial^2 T_{\mathrm{s}}}{\partial x^2}+\frac{\partial^2 T_{\mathrm{s}}}{\partial y^2}\right)-h\left(T_{\mathrm{s}}-T_{\mathrm{nf}}\right) \tag{5}$$

According to the schematic view of the problem physics, shown in Fig. 1, the boundary conditions are:

$$\forall x,y\left|x^2+(y-e)^2=r_{\mathrm{i}}^2\Rightarrow u=v=0,\ T=T_{\mathrm{h}}\right. \tag{6a}$$

$$\forall x,y\left|x^2+y^2=r_{\mathrm{o}}^2\Rightarrow u=v=0,T=T_{\mathrm{c}}\right. \tag{6b}$$

Bulk properties of the water–NEPCM particle mixture

The following weighted function is utilized for achieving the density of mixture [45]:

$$\rho_{\mathrm{nf}}=(1-\phi)\rho_{\mathrm{bf}}+\phi\rho_{\mathrm{p}} \tag{7}$$

The subscripts p and bf, respectively, represent the NEPCM particles and the base fluid. The total density of the nanoparticles is computed as [45]:

$$\rho_{\mathrm{p}}=\frac{(1+\iota)\rho_{\mathrm{co}}\rho_{\mathrm{sh}}}{\rho_{\mathrm{sh}}+\iota\rho_{\mathrm{co}}} \tag{8}$$

Here, ρ_{sh} shows the density of the shell of nanoparticles, while ρ_{co} indicates the density of the core of the nanoparticles. The mass ratio (core/shell) is denoted by ι, and $\iota\approx0.447$ [29]. The specific heat capacity of the mixture is obtained using the following weighted function [46, 47]:

$$C_{\mathrm{p,\,nf}}=\frac{(1-\phi)\left(\rho C_{\mathrm{p}}\right)_{\mathrm{bf}}+\phi\left(\rho C_{\mathrm{p}}\right)_{\mathrm{p,eff}}}{\rho_{\mathrm{nf}}} \tag{9}$$

When the core of NEPCM particles does not undergo the melting, $C_{\mathrm{p,p,eff}}$ can be measured by the below relation [45]:

$$C_{\mathrm{p,p}}=\frac{\left(C_{\mathrm{p,\,co}}+\iota C_{\mathrm{p,\,sh}}\right)\rho_{\mathrm{co}}\rho_{\mathrm{sh}}}{\left(\rho_{\mathrm{sh}}+\iota\rho_{\mathrm{co}}\right)\rho_{\mathrm{p}}} \tag{10}$$

It is worth mentioning that the specific heat capacity of the core of encapsulated nanoparticles is the mean of the heat capacities of the solid and fluid phases. Since the core of NEPCM particles can be melted, the latent heat of solid–liquid phase change needs to be considered in computations of the nanoparticle's specific heat capacity. The sinusoidal profile has the advantages of good convergence and is adopted in the present study as [45, 48]:

$$C_{\mathrm{p,p,eff}}=C_{\mathrm{p,p}}+\left\{\frac{\pi}{2}\cdot\left(\frac{h_{\mathrm{sf}}}{T_{\mathrm{Mr}}}-C_{\mathrm{p,p}}\right)\cdot\sin\left(\pi\frac{T-T_{\mathrm{f}}+T_{\mathrm{Mr}}/2}{T_{\mathrm{Mr}}}\right)\right\}\gamma \tag{11a}$$

Table 1 Thermophysical properties of the components of the mixture [29, 59]

Materials	k/W m^{-1} K^{-1}	ρ/ kg m^{-3}	C_{p}/kJ kg^{-1} K^{-1}	B/K^{-1}	μ/kg m^{-1} s^{-1}
Host fluid	0.613	997.1	4179	21.0×10^{-5}	8.9×10^{-4}
Glass balls	1.05	2700	840	0.90×10^{-5}	–
PU	–	786	1317.7	–	–
Nonadecane	–	721	2037	–	–

$$\gamma = \begin{cases} 0 & T < T_f - T_{Mr}/2 \\ 1 & T_f - T_{Mr}/2 < T < T_f + T_{Mr}/2 \\ 0 & T > T_f + T_{Mr}/2 \end{cases} \quad (11b)$$

The temperature interval, i.e., T_{Mr}, is the temperature bond of the phase change. The apparent and latent heat of the nanoparticles was taken into account using the above profiles. It is clear that the latent heat of phase change is a function of T_{Mr} [45, 48], and the middle of the phase change profile is the fusion temperature T_f:

The coefficient of volume expansion of the water–NEPCM particle mixture is [47]:

$$\beta_{nf} = (1-\phi)\beta_{bf} + \phi\beta_p \quad (12)$$

In addition, the following linear functions can be used to obtain the dynamic viscosity and thermal conductivity of water–NEPCM particle mixture [46, 47]:

$$\mu_{nf} = \mu_{bf}(1 + Nv\phi) \quad (13a)$$

$$k_{nf} = k_{bf}(1 + Nc\phi) \quad (13b)$$

Nv and *Nc* of the above relations represent the numbers of dynamic viscosity and thermal conductivity, respectively. These linear relations were confirmed by benchmark studies of Buongiorno et al. [49] and Venerus et al. [50] as a comprehensive experiment at various laboratories around the world. Later Zaraki et al. [51] computed and reported the values of *Nc* and *Nv* for different types of nanofluids. The values of *Nv* and *Nc* were also discussed in [52, 53] for nanoenhanced PCMs and hybrid nanofluids.

Non-dimensionalizing the equations and boundary conditions

The non-dimensionalization technique facilitates the study of the problem at hand and reduces the number of free parameters. In the non-dimensionalization technique, an appropriate combination of the fluid properties and flow characteristics needs to be found. The following dimensionless parameters are employed to non-dimensionalizing the equations and boundary conditions:

$$X = \frac{x}{L}, \quad Y = \frac{y}{L}, \quad R_i = \frac{r_i}{L}, \quad R_o = \frac{r_o}{L}, \quad Ec = \frac{e}{L}, \quad U = \frac{uL}{\alpha_{bf}},$$
$$V = \frac{vL}{\alpha_{bf}}, \quad P = \frac{pL^2}{\rho_{bf}\alpha_{bf}^2}, \quad \theta_{nf} = \frac{T_{nf} - T_c}{\Delta T}, \quad \theta_s = \frac{T_s - T_c}{\Delta T} \quad (14)$$

where $\Delta T = T_h - T_c$ and $L = r_o - r_i$. Invoking the non-dimensional parameters, the governing non-dimensional equations and the corresponding boundary conditions are derived as follows:

$$\frac{\partial U}{\partial X} + \frac{\partial V}{\partial Y} = 0 \quad (15)$$

$$\varepsilon^{-2}\left(\frac{\rho_{nf}}{\rho_{bf}}\right)\left(U\frac{\partial U}{\partial X} + V\frac{\partial U}{\partial Y}\right) = -\frac{\partial P}{\partial X} + Pr\,\varepsilon^{-1}\left(\frac{\mu_{nf}}{\mu_{bf}}\right)\left(\frac{\partial^2 U}{\partial X^2} + \frac{\partial^2 U}{\partial Y^2}\right) - \frac{Pr}{Da}\left(\frac{\mu_{nf}}{\mu_{bf}}\right)U \quad (16)$$

$$\varepsilon^{-2}\left(\frac{\rho_{nf}}{\rho_{bf}}\right)\left(U\frac{\partial V}{\partial X} + V\frac{\partial V}{\partial Y}\right) = -\frac{\partial P}{\partial Y} + Pr\,\varepsilon^{-1}\left(\frac{\mu_{nf}}{\mu_{bf}}\right)\left(\frac{\partial^2 V}{\partial X^2} + \frac{\partial^2 V}{\partial Y^2}\right) + Ra\cdot Pr\left(\frac{\beta_{nf}}{\beta_{bf}}\right)\theta - \frac{Pr}{Da}\left(\frac{\mu_{nf}}{\mu_{bf}}\right)V \quad (17)$$

where, respectively, Rayleigh number *Ra*, Prandtl number *Pr* and Darcy number *Da* are:

$$Ra = \frac{g\rho_{bf}\beta_{bf}\Delta T L^3}{\alpha_{bf}\mu_{bf}}, \quad Pr = \frac{\mu_{bf}}{\rho_{bf}\alpha_{bf}}, \; Da = \frac{K}{L^2} \quad (18)$$

Also,

$$\left(\frac{\rho_{nf}}{\rho_{bf}}\right) = (1-\phi) + \phi\left(\frac{\rho_p}{\rho_{bf}}\right), \quad \left(\frac{\beta_{nf}}{\beta_{bf}}\right) = (1-\phi) + \phi\left(\frac{\beta_p}{\beta_{bf}}\right) \quad (19)$$

Here, it is assumed that the thermal expansion of the NEPCM nanoparticles is similar to the base fluid as $\beta_p = \beta_{bf}$, and hence, $\beta_{nf}/\beta_{bf} = 1$. The non-dimensional heat equation in the NEPCM suspension inside the porous pores is obtained as:

$$Cr\left(U\frac{\partial\theta_{nf}}{\partial X} + V\frac{\partial\theta_{nf}}{\partial Y}\right) = \varepsilon k_{r,nf}\left(\frac{\partial^2\theta_{nf}}{\partial X^2} + \frac{\partial^2\theta_{nf}}{\partial Y^2}\right) + H(\theta_s - \theta_{nf}) \quad (20)$$

where

$$k_{r,nf} = \left(\frac{k_{nf}}{k_{bf}}\right), \; Cr = \frac{(\rho C_p)_{nf}}{(\rho C_p)_{bf}} = (1-\phi) + \phi\lambda + \frac{\phi}{\delta\, Ste}f \quad (21)$$

λ, δ and *Ste* of the above relations, respectively, are:

$$\lambda = \frac{(C_{p,co} + \iota C_{p,sh})\rho_{co}\rho_{sh}}{(\rho C_p)_{bf}(\rho_{sh} + \iota\rho_{co})}, \; \delta = \frac{T_{Mr}}{\Delta T}, \; Ste = \frac{(\rho C_p)_{bf}(\rho_{sh} + \iota\rho_{co})\Delta T}{(h_{sf}\rho_{co}\rho_{sh})(1+\iota)} \quad (22)$$

The non-dimensional fusion function, i.e., *f*, is:

$$f = \frac{\pi}{2}\sin\left(\frac{\pi}{\delta}(\theta - \theta_f + \delta/2)\right)\sigma \quad (23a)$$

$$\sigma = \begin{cases} 0 & \theta < \theta_{\mathrm{f}} - \delta/2 \\ 1 & \theta_{\mathrm{f}} - \frac{\delta}{2} < \theta < \theta_{\mathrm{f}} + \delta/2 \\ 0 & \theta > \theta_{\mathrm{f}} + \delta/2 \end{cases} \tag{23b}$$

Here, θ_{f}, the non-dimensional fusion temperature, is:

$$\theta_{\mathrm{f}} = \frac{T_{\mathrm{f}} - T_{\mathrm{c}}}{\Delta T} \tag{24}$$

The energy balance equation for the solid matrix in the dimensionless coordinates can be written as follows:

$$0 = (1-\varepsilon)K_{\mathrm{r,s}}\left(\frac{\partial^2\theta_{\mathrm{s}}}{\partial X^2} + \frac{\partial^2\theta_{\mathrm{s}}}{\partial Y^2}\right) - H\left(\theta_{\mathrm{s}} - \theta_{\mathrm{nf}}\right) \tag{25}$$

where

$$K_{\mathrm{r,s}} = \frac{k_{\mathrm{s}}}{k_{\mathrm{bf}}}, H = \frac{hL^2}{k_{\mathrm{bf}}} \tag{26}$$

Eventually, the boundary conditions are transformed into a non-dimensional form as:

$$\forall X, Y \left| X^2 + (Y - Ec)^2 = R_{\mathrm{i}}^2 \Rightarrow U = V = 0,\ \theta = 1 \right. \tag{27a}$$

$$\forall X, Y \left| X^2 + Y^2 = R_{\mathrm{o}}^2 \Rightarrow U = V = 0,\ \theta = 0 \right. \tag{27b}$$

The local Nusselt numbers on the hot, inner cylinder are determined as follows:

$$Nu_{\mathrm{nf,l}} = k_{\mathrm{r,nf}}\left(\frac{\partial\theta_{\mathrm{nf}}}{\partial n}\right)_{\mathrm{C_i}} \tag{28a}$$

$$Nu_{\mathrm{s,l}} = K_{\mathrm{r,s}}\left(\frac{\partial\theta_{\mathrm{s}}}{\partial n}\right)_{\mathrm{C_i}} \tag{28b}$$

The average Nusselt numbers are defined as:

$$Nu_{\mathrm{nf}} = \frac{1}{2\pi}\int_0^{2\pi} Nu_{\mathrm{nf,l}}\mathrm{d}\omega \tag{29a}$$

$$Nu_{\mathrm{s}} = \frac{1}{2\pi}\int_0^{2\pi} Nu_{\mathrm{s,l}}\mathrm{d}\omega \tag{29b}$$

The total heat transfer rate, Q_{t}, can be introduced as:

$$Q_{\mathrm{t}} = \varepsilon Nu_{\mathrm{nf}} + (1-\varepsilon)Nu_{\mathrm{s}} \tag{30}$$

The non-dimensional streamline is introduced in the following way to visualize the fluid motion:

$$\frac{\partial^2\Psi}{\partial X^2} + \frac{\partial^2\Psi}{\partial Y^2} = -\left(\frac{\partial V}{\partial X} - \frac{\partial U}{\partial Y}\right) \tag{31}$$

where the solid walls are considered as Dirichlet condition with $\Psi = 0$.

Numerical approach and mesh test

The Galerkin finite element method is used to solve the dimensionless governing equations (continuity, momentum and energy) with the mentioned boundary conditions. The computational fluid–porous domain is discretized using non-uniform structural mesh, as explained in Fig. 2. The dimensionless governing equations for the velocity and temperature fields are completely coupled utilizing the damped Newton scheme. Next, then solution for the equivalent linear algebraic equations is obtained by the parallel sparse direct solver.

Finite element method uses the interpolate (or shape) functions $\{\gamma_{\mathrm{m}}\}_{\mathrm{m=1}}^{N}$ to expand the governing variables as follows:

$$U \approx \sum_{\mathrm{m=1}}^{N} U_{\mathrm{m}}\gamma_{\mathrm{m}}(X,Y),\ V \approx \sum_{\mathrm{m=1}}^{N} V_{\mathrm{m}}\gamma_{\mathrm{m}}(X,Y),\ P \approx \sum_{\mathrm{m=1}}^{N} P_{\mathrm{m}}\gamma_{\mathrm{m}}(X,Y),$$
$$\theta_{\mathrm{nf}} \approx \sum_{\mathrm{m=1}}^{N} \theta_{\mathrm{nf_m}}\gamma_{\mathrm{m}}(X,Y),\ \theta_{\mathrm{s}} \approx \sum_{\mathrm{m=1}}^{N} \theta_{\mathrm{s_m}}\gamma_{\mathrm{m}}(X,Y),\ \Psi \approx \sum_{\mathrm{m=1}}^{N} \Psi_{\mathrm{m}}\gamma_{\mathrm{m}}(X,Y) \tag{32}$$

The residual equations for the above variables at each element can be achieved by invoking the Galerkin approach:

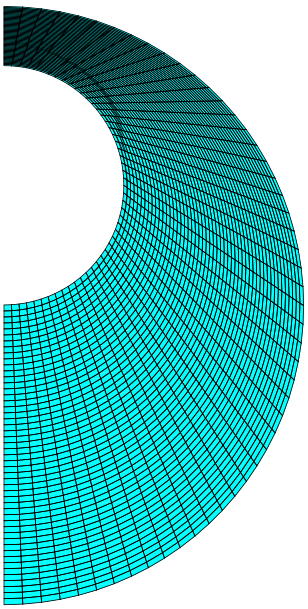

Fig. 2 Uniform structural mesh

$$R_{\mathrm{i}}^{1} \approx \varepsilon^{-2}\left(\frac{\rho_{\mathrm{nf}}}{\rho_{\mathrm{bf}}}\right)\sum_{\mathrm{m}=1}^{N} U_{\mathrm{m}}\int\left[\left(\sum_{\mathrm{m}=1}^{N} U_{\mathrm{m}}\gamma_{\mathrm{m}}\right)\frac{\partial\gamma_{\mathrm{m}}}{\partial X}+\left(\sum_{\mathrm{k}=1}^{N} V_{\mathrm{m}}\gamma_{\mathrm{m}}\right)\frac{\partial\gamma_{\mathrm{m}}}{\partial Y}\right]\gamma_{\mathrm{i}}\mathrm{d}X\mathrm{d}Y$$
$$-\sum_{\mathrm{m}=1}^{N}\int\left(\sum_{\mathrm{m}=1}^{N} P_{\mathrm{m}}\gamma_{\mathrm{m}}\right)\frac{\partial\gamma_{\mathrm{m}}}{\partial X}\gamma_{\mathrm{i}}\mathrm{d}X\mathrm{d}Y+Pr\varepsilon^{-1}\left(\frac{\mu_{\mathrm{nf}}}{\mu_{\mathrm{bf}}}\right)\sum_{\mathrm{m}=1}^{N} U_{\mathrm{m}}\int\left[\frac{\partial\gamma_{\mathrm{m}}}{\partial Y}\frac{\partial\gamma_{\mathrm{i}}}{\partial Y}\right]\mathrm{d}X\mathrm{d}Y \tag{33a}$$
$$+Pr\varepsilon^{-1}\left(\frac{\mu_{\mathrm{nf}}}{\mu_{\mathrm{bf}}}\right)\sum_{\mathrm{m}=1}^{N} U_{\mathrm{m}}\int\left[\frac{\partial\gamma_{\mathrm{m}}}{\partial X}\frac{\partial\gamma_{\mathrm{i}}}{\partial X}\right]\mathrm{d}X\mathrm{d}Y-\frac{Pr}{Da}\left(\frac{\mu_{\mathrm{nf}}}{\mu_{\mathrm{bf}}}\right)\int\left(\sum_{\mathrm{m}=1}^{N} U_{\mathrm{m}}\gamma_{\mathrm{m}}\right)\gamma_{\mathrm{i}}\mathrm{d}X\mathrm{d}Y$$

$$R_{\mathrm{i}}^{2} \approx \varepsilon^{-2}\left(\frac{\rho_{\mathrm{nf}}}{\rho_{\mathrm{bf}}}\right)\sum_{\mathrm{m}=1}^{N} V_{\mathrm{m}}\int\left[\left(\sum_{\mathrm{m}=1}^{N} U_{\mathrm{m}}\gamma_{\mathrm{m}}\right)\frac{\partial\gamma_{\mathrm{m}}}{\partial X}+\left(\sum_{\mathrm{k}=1}^{N} V_{\mathrm{m}}\gamma_{\mathrm{m}}\right)\frac{\partial\gamma_{\mathrm{m}}}{\partial Y}\right]\gamma_{\mathrm{i}}\mathrm{d}X\mathrm{d}Y$$
$$-\sum_{\mathrm{m}=1}^{N}\int\left(\sum_{\mathrm{m}=1}^{N} P_{\mathrm{m}}\gamma_{\mathrm{m}}\right)\frac{\partial\gamma_{\mathrm{i}}}{\partial Y}\mathrm{d}X\mathrm{d}Y+Pr\varepsilon^{-1}\left(\frac{\mu_{\mathrm{nf}}}{\mu_{\mathrm{bf}}}\right)\sum_{\mathrm{m}=1}^{N} V_{\mathrm{m}}\int\left[\frac{\partial\gamma_{\mathrm{m}}}{\partial X}\frac{\partial\gamma_{\mathrm{i}}}{\partial X}\right]\mathrm{d}X\mathrm{d}Y \tag{33b}$$
$$+Pr\varepsilon^{-1}\left(\frac{\mu_{\mathrm{nf}}}{\mu_{\mathrm{bf}}}\right)\sum_{\mathrm{m}=1}^{N} V_{\mathrm{m}}\int\left[\frac{\partial\gamma_{\mathrm{m}}}{\partial Y}\frac{\partial\gamma_{\mathrm{i}}}{\partial Y}\right]\mathrm{d}X\mathrm{d}Y-\frac{Pr}{Da}\left(\frac{\mu_{\mathrm{nf}}}{\mu_{\mathrm{bf}}}\right)\int\left(\sum_{\mathrm{m}=1}^{N} V_{\mathrm{m}}\gamma_{\mathrm{m}}\right)\gamma_{\mathrm{i}}\mathrm{d}X\mathrm{d}Y$$
$$+Ra\cdot Pr\left(\frac{\beta_{\mathrm{nf}}}{\beta_{\mathrm{bf}}}\right)\int\left(\sum_{\mathrm{m}=1}^{N}\theta_{\mathrm{nf_m}}\gamma_{\mathrm{m}}\right)\gamma_{\mathrm{i}}\mathrm{d}X\mathrm{d}Y$$

$$R_{\mathrm{i}}^{3} \approx \sum_{\mathrm{m}=1}^{N} U_{\mathrm{m}}\int\frac{\partial\gamma_{\mathrm{m}}}{\partial X}\gamma_{\mathrm{i}}\mathrm{d}X\mathrm{d}Y+\sum_{\mathrm{m}=1}^{N} V_{\mathrm{m}}\int\frac{\partial\gamma_{\mathrm{m}}}{\partial Y}\gamma_{\mathrm{i}}\mathrm{d}X\mathrm{d}Y \tag{33c}$$

$$R_{\mathrm{i}}^{4} \approx Cr\sum_{\mathrm{m}=1}^{N}\theta_{\mathrm{nf_m}}\int\left[\left(\sum_{\mathrm{m}=1}^{N} U_{\mathrm{m}}\gamma_{\mathrm{m}}\right)\frac{\partial\gamma_{\mathrm{m}}}{\partial X}+\left(\sum_{\mathrm{m}=1}^{N} V_{\mathrm{m}}\gamma_{\mathrm{m}}\right)\frac{\partial\gamma_{\mathrm{m}}}{\partial Y}\right]\gamma_{\mathrm{m}}\mathrm{d}X\mathrm{d}Y+\varepsilon k_{r,nf}\sum_{\mathrm{m}=1}^{N}\theta_{\mathrm{nf_m}}$$
$$\int\left[\frac{\partial\gamma_{\mathrm{m}}}{\partial X}\frac{\partial\gamma_{\mathrm{i}}}{\partial X}+\frac{\partial\gamma_{\mathrm{m}}}{\partial Y}\frac{\partial\gamma_{\mathrm{i}}}{\partial Y}\right]\mathrm{d}X\mathrm{d}Y+H\left[\int\left(\sum_{\mathrm{m}=1}^{N}\theta_{\mathrm{s_m}}\gamma_{\mathrm{m}}\right)\right.$$
$$\left.-\int\left(\sum_{\mathrm{m}=1}^{N}\theta_{\mathrm{nf_m}}\gamma_{\mathrm{m}}\right)\right]\gamma_{\mathrm{i}}\mathrm{d}X\mathrm{d}Y \tag{33d}$$

$$R_{\mathrm{i}}^{5} \approx (1-\varepsilon)K_{\mathrm{r,s}}\sum_{\mathrm{m}=1}^{N}\theta_{\mathrm{s_k}}\int\left[\frac{\partial\gamma_{\mathrm{m}}}{\partial X}\frac{\partial\gamma_{\mathrm{i}}}{\partial X}+\frac{\partial\gamma_{\mathrm{m}}}{\partial Y}\frac{\partial\gamma_{\mathrm{i}}}{\partial Y}\right]\mathrm{d}X\mathrm{d}Y$$
$$-H\left[\int\left(\sum_{\mathrm{m}=1}^{N}\theta_{\mathrm{s_m}}\gamma_{\mathrm{m}}\right)-\int\left(\sum_{\mathrm{m}=1}^{N}\theta_{\mathrm{nf_m}}\gamma_{\mathrm{m}}\right)\right]\gamma_{\mathrm{i}}\mathrm{d}X\mathrm{d}Y \tag{33e}$$

$$R_{\mathrm{i}}^{6} \approx \sum_{\mathrm{m}=1}^{N}\Psi_{\mathrm{m}}\int\left[\frac{\partial\gamma_{\mathrm{m}}}{\partial X}\frac{\partial\gamma_{\mathrm{i}}}{\partial X}+\frac{\partial\gamma_{\mathrm{m}}}{\partial Y}\frac{\partial\gamma_{\mathrm{i}}}{\partial Y}\right]\mathrm{d}X\mathrm{d}Y$$
$$+\int\left[\left(\sum_{\mathrm{m}=1}^{N} U_{\mathrm{m}}\gamma_{\mathrm{m}}\right)\frac{\partial\gamma_{\mathrm{m}}}{\partial Y}-\left(\sum_{\mathrm{k}=1}^{N} V_{\mathrm{m}}\gamma_{\mathrm{m}}\right)\frac{\partial\gamma_{\mathrm{m}}}{\partial X}\right]\gamma_{\mathrm{i}}\mathrm{d}X\mathrm{d}Y \tag{33f}$$

Gaussian quadrature with second-order accuracy is applied to integrate the above integral residuals. Newton method using the parallel sparse direct solver (PARDISO) is also utilized to solve the residual equations, iteratively [54–56]. The error convergence for each of the dependent variables is not more than 10^{-5}.

The mesh test for the present work to check the mesh stability is shown in Table 2. The results of the mesh

Table 2 Mesh independence test for Q_{t} and $|\Psi|_{\max}$ on the hot inner cylinder at $Ra=10^{6}$, $Da=10^{-3}$, $\phi=0.03$, $\theta_{\mathrm{f}}=0.5$, $H=1000$, $Ste=0.2$, $\varepsilon=0.9$, $Ec=-0.67$ and $Rr=2.5$

Case number/*i*	Number of elements	Q_{t}	Δ_1	$\lvert\Psi\rvert_{\max}$	Δ_2
1	90×90	10.527	–	29.699	0
2	100×100	10.532	0.0475	29.703	0.0130
3	120×120	10.530	0.0190	29.732	0.0976
4	140×140	10.487	0.4084	29.391	1.1460
5	160×160	10.529	0.4005	29.749	1.2168

$\Delta_1 = \left||\Psi|_{\max,\mathrm{i}+1} - |\Psi|_{\max,\mathrm{i}}\right| / |\Psi|_{\max,\mathrm{i}}$

$\Delta_2 = \left|Q_{\mathrm{t,i}+1} - Q_{\mathrm{t,i}}\right| / Q_{\mathrm{t,i}}$

Table 3 Comparison between the results of the present study and the study carried out by Matin and Pop [57]

Volume fraction	Present work	Matin and Pop [57]	Difference/%
0.010	5.60	5.66	1.07
0.015	5.78	5.81	0.51
0.020	5.86	5.89	0.51
0.025	6.04	5.97	1.15
0.030	6.07	6.02	0.82

Table 4 Average Nusselt number computed in the current research and that of Nithiarasu et al. [58]

Da	*Ra*	ε	Present study	[58]
10^{-6}	10^{7}	0.4	1.078	1.078
10^{-4}	10^{7}	0.9	9.322	9.202
10^{-2}	10^{4}	0.4	1.360	1.408
10^{-2}	10^{5}	0.9	3.92	3.91

independency test are the total hat transfer rate on the hot inner cylinder and absolute maximum stream function for the case of $Ra=10^5$, $Da=10^{-3}$, $Pr=6.2$, $Ec=0.67$, $Ste=0.2$, $\varepsilon=0.65$, $\lambda=0.322$, $Nv=12.5$, $Nc=23.8$, $\delta=0.05$, $\phi=0.05$, $H=1000$, $\theta_f=0.5$ and $Rr=1.67$. The information about this parameter will be introduced in the next section. The number of elements started with 90×90 and finished by 160×160. The mesh 140×140 has been chosen for analysis of the results. Although the errors of the grid size of 140×140 are not the lowest, the phase change zone, represented in Results and discussion section, is better modeled with this grid.

The outcomes of the present research are compared with two works published to verify the accuracy and the correctness of the current code. Here, the average Nusselt numbers of the current study and those reported by Habibi and Pop [57] are compared. Habibi and Pop [57] conducted the study of natural convection flow inside an annulus occupied by Cu–water nanofluid. The average Nusselt numbers for the different values of volume fraction of the nanoparticles of the current calculations and those presented by Habibi and Pop [57] are tabulated in Table 3. Clearly, an entirely satisfactory agreement between the outcomes of Habibi and Pop [57] and ours is found. In the second stage, the results of the current work are compared with the outcomes of Nithiarasu et al. [58] in terms of heat transfer rate. In the work of Nithiarasu et al. [58], the study of a porous square cavity was conducted for a cavity with insulated walls at top and bottom and isothermal sidewalls. The left and right vertical sidewalls for the cavity were at high and low isothermal temperatures. The results of the comparison for average Nusselt number are summarized in Table 4 when $Pr=1$. As given in Table 4, excellent matching is observed.

Results and discussion

The current study deals with the hydrodynamic and thermal characteristics of the water–NEPCM particle mixture inside a porous annulus of horizontal cylinders. The local thermal non-equilibrium condition between the phases of the porous medium is considered to be established. The impacts of different involved parameters on the flow and thermal fields of the mixture are investigated. These alterable parameters are Rayleigh number ($10^4\le Ra\le10^6$), Stefan number ($0.2\le Ste<\infty$), melting point temperature of the core ($0.05\le\theta_f\le0.95$), the concentration of the NEPCM particles ($0.0\le\phi\le5\%$), radius ratio ($1.67\le Rr\le2.5$), eccentricity ($-0.67\le Ec\le0.67$), Darcy number ($10^{-4}\le Da\le10^{-1}$), porosity ($0.3\le\varepsilon\le0.9$) and interface heat transfer coefficient ($1\le H\le1000$). The constant parameters are $Nv=12.5$, $Nc=23.8$, $Pr=6.2$, $\delta=0.05$ and $\lambda=0.32$.

Since the geometry is symmetrical about *Y*-axis, only half of the right geometry is considered to show the results. Figure 3 represents the isotherms of the fluid and solid phases of the porous medium, streamlines and the heat capacity ratio at fixed parameters such as $Da=0.1$, $\phi=0.05$, $\theta_f=0.1$, $Ste=0.2$, $\varepsilon=0.8$, $Ec=0.67$, $Rr=2.5$, $\delta=0.05$, $\lambda=0.322$, $Nv=12.5$, $Nc=23.8$, $Pr=6.2$ with different Rayleigh numbers (*Ra*) and the interface heat transfer coefficient (*H*). As shown in Fig. 3, the isotherms are distributed as a crescent shape around the hot inner cylinder for two phases, solid and fluid, where it clustered above the hot inner cylinder and dispersed under it due to the eccentricity of the hot cylinder. Figure 3a shows that there is a noticeable difference in isothermal lines between solid and fluid phases, depicting the non-equilibrium thermal condition between the two phases. This discrepancy is attributed to the low value of *H*.

As shown in Fig. 3, the streamlines move in a clockwise direction. The suspension is heated besides the hot inner cylinder and moves up toward the cold outer one to be cooled; therefore, a single vortex can be seen with maximum strength $|\Psi|_{max}=50.83$. The phase change ribbon divides the whole domain into three sub-domains; melting zone, phase change zone and solidification zone. In the melting zone, the space between the hot cylinder and the ribbon, and the core of the NEPCM particles are fully melted. In contrast, in the area limited by the ribbon and the outer cylinder, i.e., solidification zone, the core of the NEPCM particles is in the solidification mode. Thus, it is evident that the NEPCM particles experience the phase change while passing through the ribbon. It can be observed that the phase change ribbon matches with isothermal line equal to the

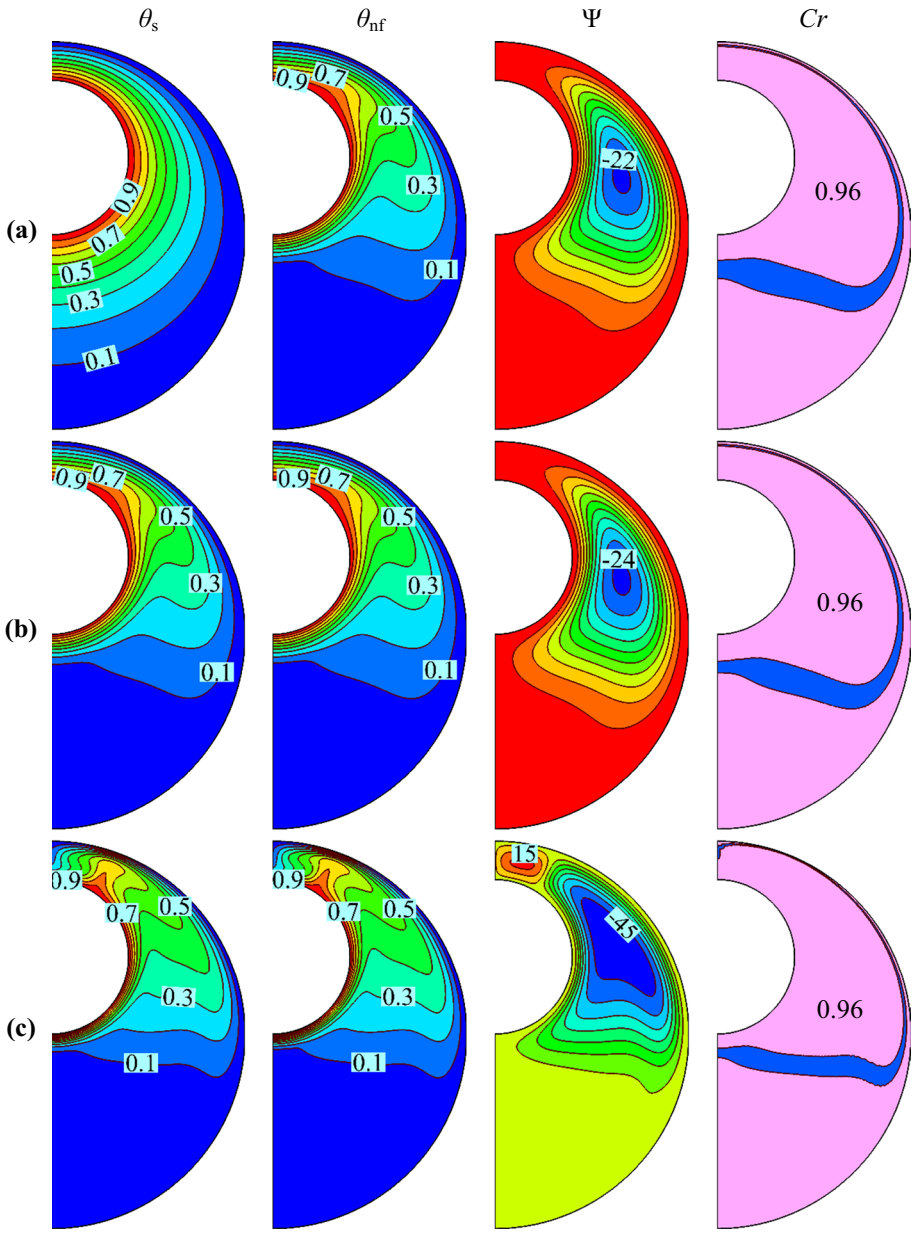

Fig. 3 Effects of Rayleigh number (Ra) and interface heat transfer coefficient (H) on the isotherms of the solid phase (θ_s), isotherms of fluid phase (θ_{nf}), streamlines (Ψ) and heat capacity ratio contour (Cr); **a** $Ra=10^5$, $H=1$, **b** $Ra=10^5$, $H=1000$ and **c** $Ra=10^6$, $H=1000$ at $Da=0.1$, $\phi=0.05$, $\theta_f=0.1$, $Ste=0.2$, $\varepsilon=0.8$, $Ec=0.67$ and $Rr=2.5$

dimensionless temperature of fusion. It is worth noting that heat capacity ratio changes inside the phase change ribbon. At the same time, it is constant outside this ribbon with a value of 0.96 as indicated.

A comparison between the first and second rows of Fig. 3, presented for different values of the H parameter, illustrates that the increase in the interface heat transfer coefficient significantly influences the temperature field of the solid matrix. At the same time, there is not a noticeable change in the isotherms of the fluid phase. In fact, when this parameter grows, the more heat is transferred from the solid phase to the fluid one. As a result, the solid and fluid phases, respectively, are heated and cooled. Then, the heat transferred to the fluid phase is conducted to the cold side by the advection mechanisms. Hence, the temperature field of the fluid does not face a significant change with the parameter of H. Moreover, as the H parameter changes to 1000, the strength of streamlines increased, due to the increase in the suspension mobility resulting from a rise in the fluid temperature. Furthermore, the incremental change in the Hs lightly narrows the phase change zone.

Finally, it can be observed that an increment in Rayleigh number (a comparison between the second and third rows of Fig. 3) intensifies the distortion of the isotherms of the fluid and solid phases, predicting the augmentation of the heat transfer rates. A detailed look in the temperature fields demonstrates that the temperatures diminish while increasing the Ra. The Rayleigh number deputizes the buoyancy

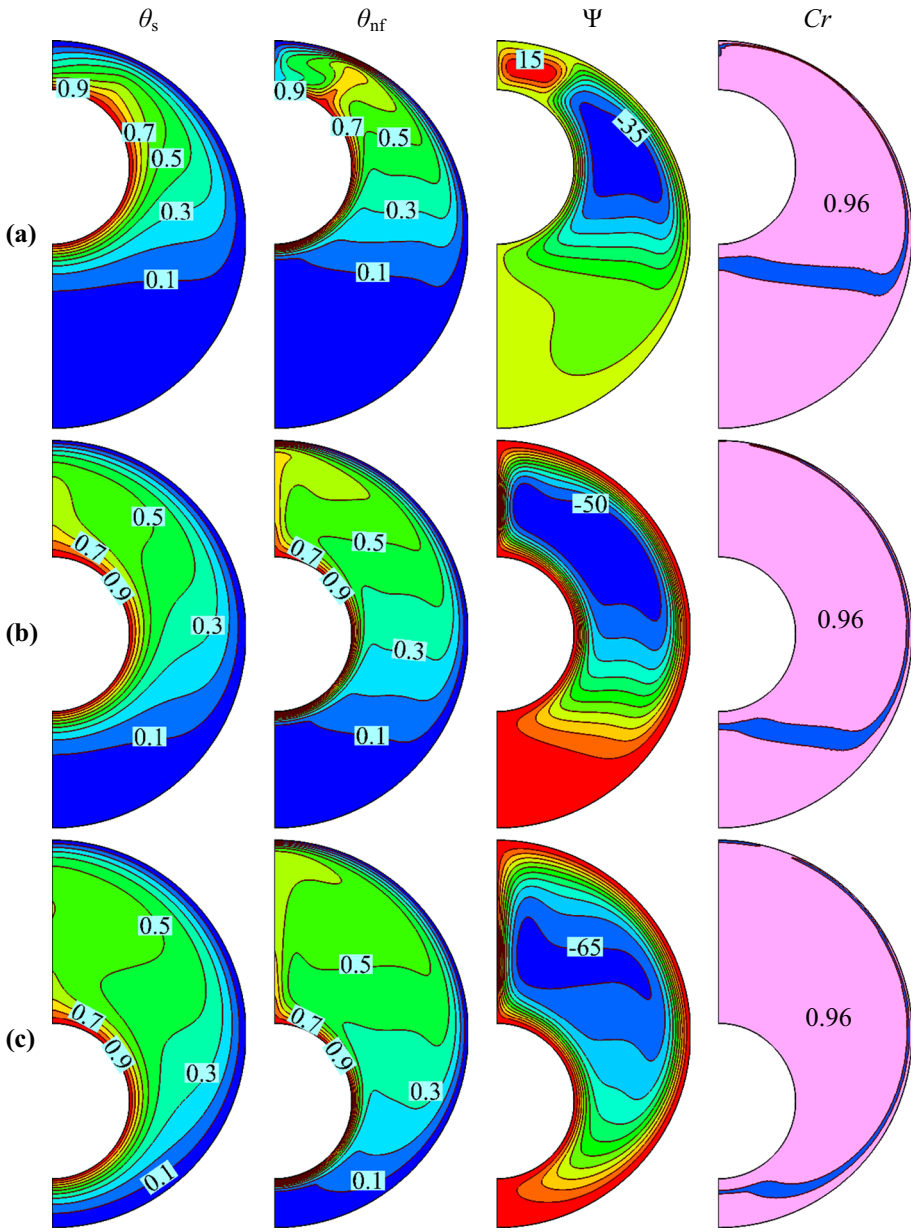

Fig. 4 Effect of the eccentricity of the hot cylinder of the isotherms of the solid phase (θ_s), isotherms of fluid phase (θ_{nf}), streamlines (Ψ) and heat capacity ratio contour (Cr); **a** $Ec=0.58$, **b** $Ec=0.0$ and **c** $Ec=-0.58$ at $Ra=10^6$, $Da=0.01$, $\phi=0.03$, $\theta_f=0.1$, $H=10$, $Ste=0.2$, $\varepsilon=0.9$ and $Rr=2.5$

force. Hence, it is evident that the flow strengthens with the Ra, as shown in Fig. 3c. The phase change ribbon became thinner and shifted upward at the higher value of Ra. High-temperature gradients produce a thin phase change ribbon of NEPCMs and vice versa.

Figure 4 shows the effect of eccentricity (Ec) on the isotherms for solid phase, isotherms for fluid phase, streamlines and heat capacity ratio (Cr). It can be seen that the position of the hot inner cylinder significantly affects the distribution of isothermal lines, streamlines and the phase change field of the NEPCM particles. When the hot cylinder shifts downward, the temperature gradients between the hot cylinder and the porous matrix are higher, leading to the augmentation of the heat transfer rates and the flow strength. Also, as the column of Cr shows, the phase change zone moves downward along with the hot cylinder and becomes thinner. Considering the flow paths and the position of the phase change zones, it can be concluded that the minimum number of the NEPCM particles undergoes the phase change when $Ec=-0.58$.

Figure 5 shows the effect of changing the Darcy number on the governing fields of the suspension flow. Decreasing Darcy number suppressed the strength of the suspension movement; therefore, the maximum stream function decreases from $|\Psi|_{max}=113.12$ to $|\Psi|_{max}=29.36$ with varying the Darcy number from 0.1 to 10^{-3}. As a matter of fact, decreasing the Da declines the permeability, resulting in the augmentation of the hydrodynamic losses. Corresponding to

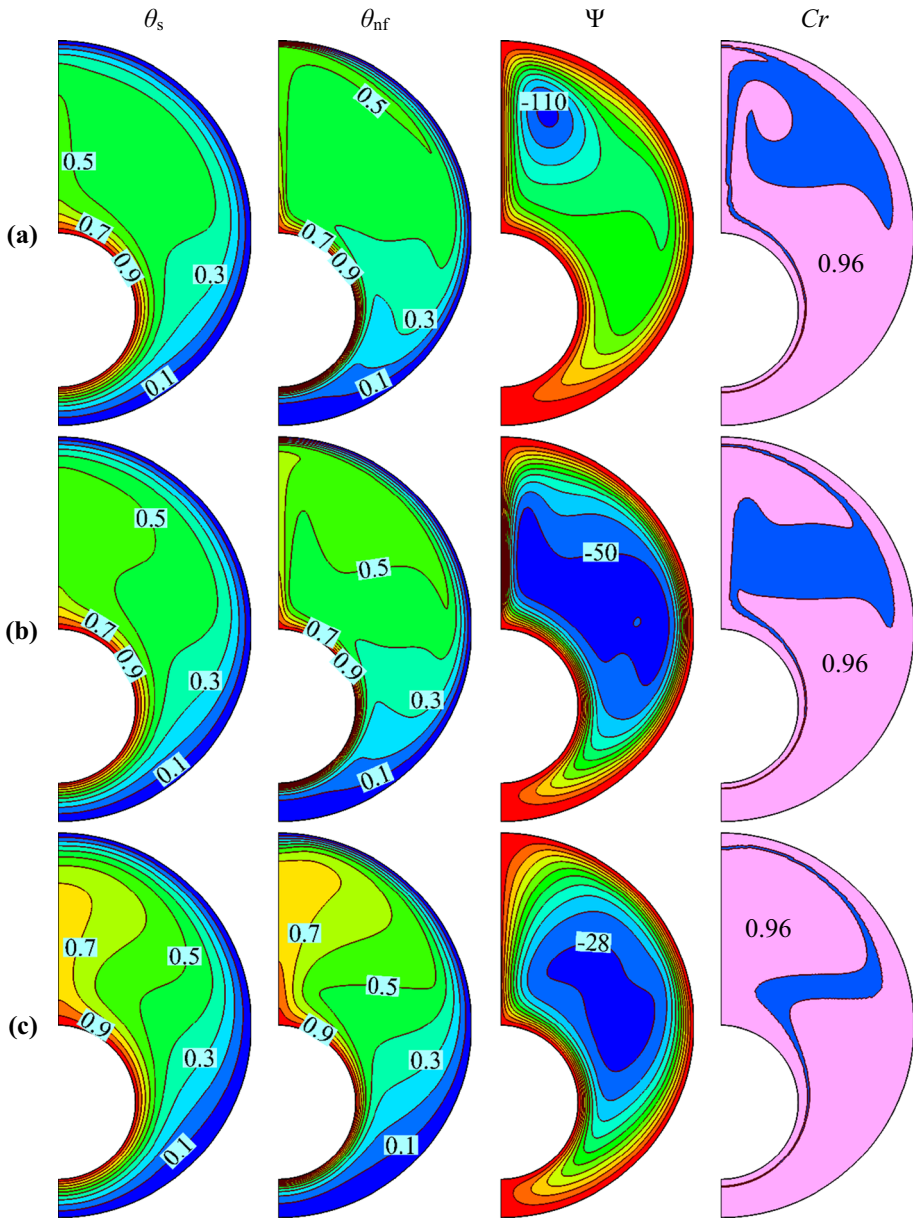

Fig. 5 Effect of Darcy number (Da) on the isotherms of the solid phase (θ_s), isotherms of fluid phase (θ_{nf}), streamlines (Ψ) and heat capacity ratio contour (Cr); **a** $Da=0.1$, **b** $Da=0.01$ and **c** $Da=0.001$ at $Ra=10^6$, $\phi=0.03$, $\theta_f=0.5$, $H=10$, $Ste=0.21$, $\varepsilon=0.9$, $Ec=-0.67$ and $Rr=2.5$

the flow fields, the reduction in the Darcy number causes the distortion of the isotherms of the fluid and solid phases to diminish, which means the decrease in the heat transfer rates. Also, it is clearly evident that the triple zones of the melting, solidification and phase change are significantly affected by the Darcy number. When the Da is high ($Da=0.1$ and 0.01), the isothermal area around the isotherms corresponding to the fusion temperature is large, leading to the formation of a thick phase change zone. It should be noted that the thickness and extension of the phase change zone, i.e., ribbon, do not indicate the number of particles affected by the melting or solidification. In fact, the number of NEPCM particles experiencing the melting/solidification depends on the position of the ribbon and the flow paths through it. Accordingly, it can be said that the Darcy number does not have a significant effect on the number of particles experiencing phase change.

Figure 6 illustrates the variation of the total heat transfer with θ_f for selected values of Stefan number in the range of $0.2 \le St \le 100$. The Q_t grows as the θ_f increases until $\theta_f \approx 0.5$, and then, it decreases with increasing θ_f. At $\theta_f=0.5$, the heat absorption by the core of NEPCM near the hot inner cylinder wall and heat release near the cold outer cylinder wall reaches a maximum rate; therefore, the maximum total heat transfer can be achieved. The results show that the total heat transfer increases with the decrease in the Stefan number. A maximum value of total heat transfer was obtained for the lowest value of the Stefan number ($Ste=0.2$). This is due to the reverse relation between latent heat and Stefan number, as shown in Eq. (22). So, when the Stefan number

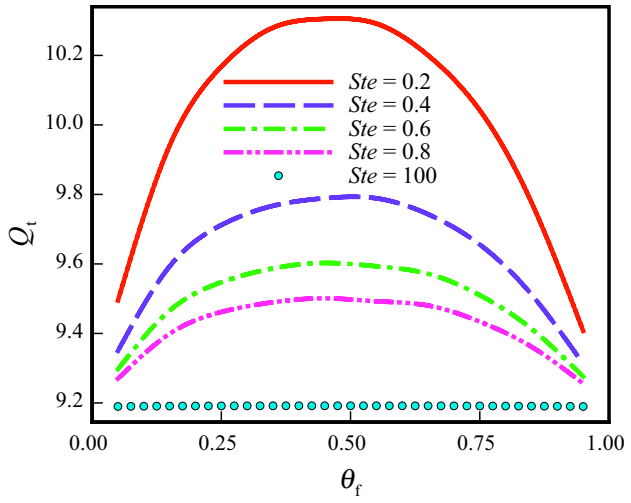

Fig. 6 Variation of total heat transfer (Q_t) with θ_f for different values of Ste at $Ra = 10^6$, $Da = 0.001$, $\phi = 0.05$, $H = 1$, $\varepsilon = 0.9$, $Ec = 0.3$ and $Rr = 2.5$

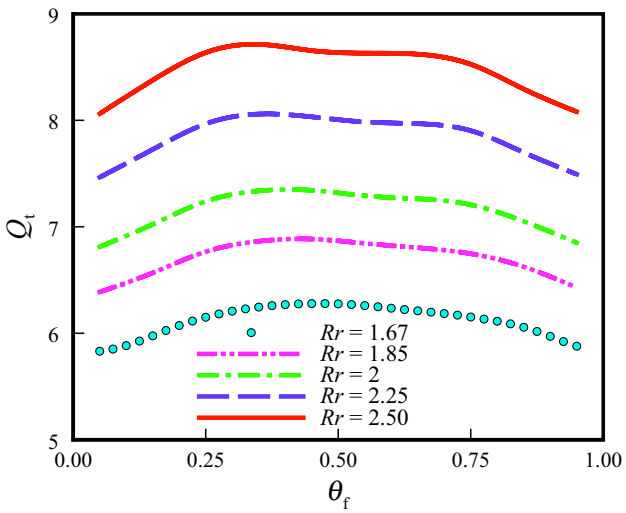

Fig. 8 Variation of total heat transfer (Q_t) with θ_f different radius ratio (Rr) at $Ra = 10^5$, $Da = 0.01$, $\phi = 0.05$, $H = 1$, $Ste = 0.2$, $\varepsilon = 0.9$ and $Ec = -0.67$

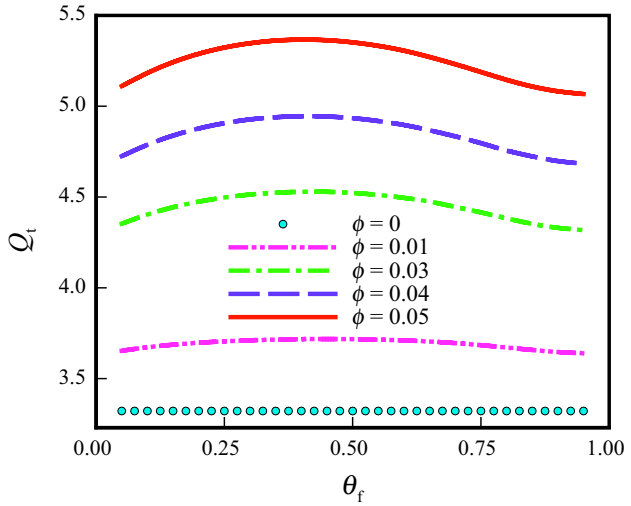

Fig. 7 Variation of total heat transfer (Q_t) with θ_f for different values of volume fraction (ϕ) $Ra = 10^6$, $Da = 0.0001$, $H = 1$, $Ste = 0.2$, $\varepsilon = 0.9$, $Ec = 0.67$ and $Rr = 2.5$

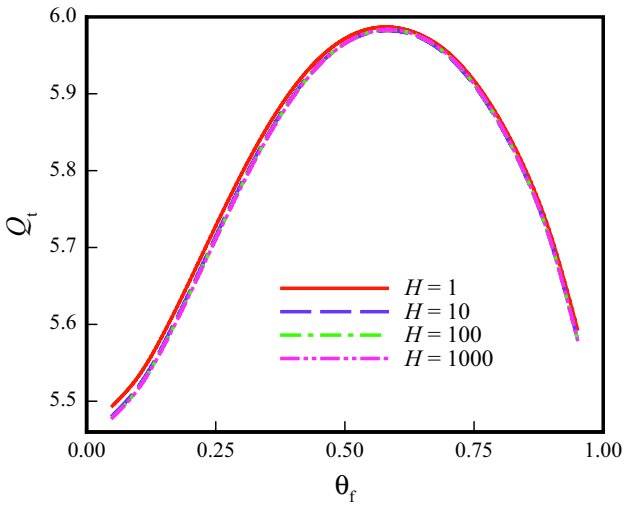

Fig. 9 Variation of total heat transfer (Q_t) with θ_f at different values of interface heat transfer coefficient (H) at $Ra = 10^6$, $Da = 0.0001$, $\phi = 0.05$, $Ste = 0.2$, $\varepsilon = 0.9$, $Ec = -0.67$ and $Rr = 2.5$

adopts a low value, the latent heat in the core of NEPCMs is at the highest value, which improves the energy storage and the heat transfer rate to the highest level. When $Ste \to \infty$, it means the zero latent heat of NEPCMs. (No phase change occurs.) At a high value of the Stefan number ($Ste = 100$), the total heat transfer is constant and equal to $Q_t = 9.191$ for all θ_f.

Figure 7 depicts the variation of total heat transfer with θ_f for different values of the nanoparticle volume fraction on NEPCM. The maximum Q_t occurs at $\theta_f = 0.4$ and minimum Q_t at $\theta_f = 0.95$. Also, the enhancement heat transfer rate is obtained for the highest value of volume fraction $\phi = 0.05$ at $\theta_f = 0.4$ compared to the pure host fluid. In fact, dispersing the NEPCM particles in the base fluid enhances the thermal conductivity and the effective heat capacity, leading to the augmentation of the heat transfer conduction and advection mechanisms, respectively.

Figure 8 shows that the increase in the radius ratio decreases Q_t. Besides, as the θ_f increases, the total heat transfer increases lightly and reaches its maximum values. Then further increases in θ_f decrease Q_t, gently. Figure 9 illustrates the influence of the thermal interaction between

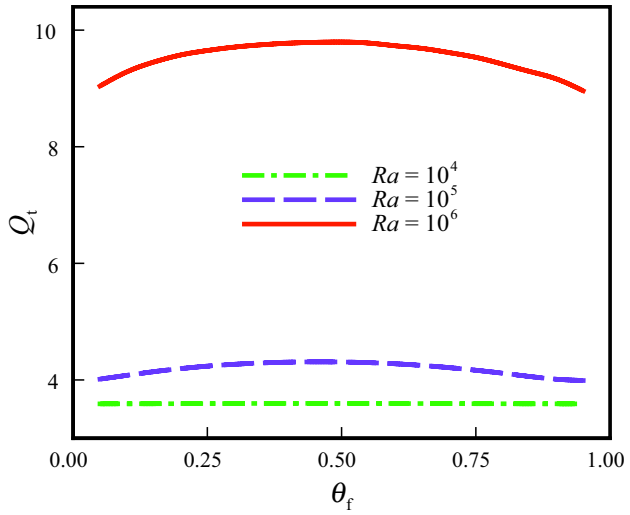

Fig. 10 Variation of total heat transfer (Q_t) with θ_f for different values of Rayleigh number (Ra) at $Da = 0.001$, $\phi = 0.05$, $H = 1$, $Ste = 0.2$, $\varepsilon = 0.8$, $Ec = 0.3$ and $Rr = 2.5$

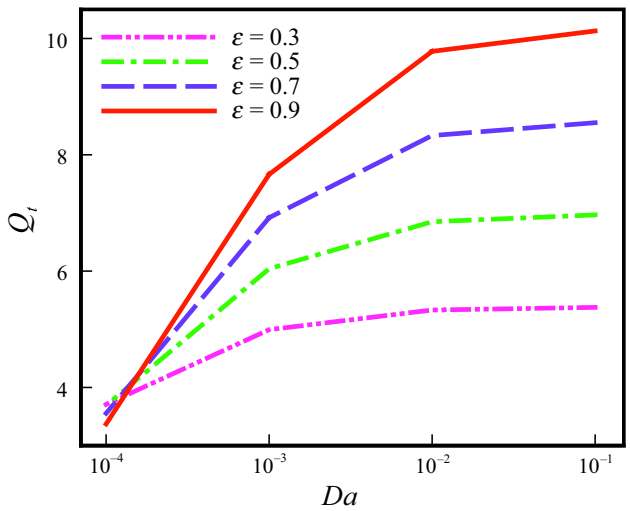

Fig. 11 Variation of the total heat transfer (Q_t) with Darcy number (Da) for different values of porosity (ε) at $Ra = 10^6$, $\phi = 0.01$, $\theta_f = 0.1$, $H = 1$, $Ste = 0.2$, $Ec = 0.3$ and $Rr = 2.5$

the suspension inside the pores and the porous matrix. The results for the total magnitude of heat transfer are plotted as a function of fusion temperature. The case of the high value of H represents the strong interaction between the suspension and porous pores, which leads to a thermal equilibrium model. As seen, when the fusion temperature is low, the difference between LTNE and LTE models is more evident compared to the case of high fusion temperature.

Figure 10 depicts the influence of the increase in the Rayleigh number on the total heat transfer for different values of θ_f. An increase in the Ra augments the buoyancy force, leading to the increment of the Q_t, as depicted in Fig. 10. The variation of the total heat transfer rate with θ_f is higher at the Rayleigh number of 10^6 compared to the other values of the Rayleigh number. This is due to that the heat capacity, including the latent heat in the advection term of the energy equation, is more effective at the higher value of Ra. A comparison among Figs. 6–10 shows that the maximum heat transfer rate does not occur in a specified fusion temperature, and this depends on the other parameters such as the Ra, Da and Ec. In fact, the position of the phase change zone and the flow paths passing through it, which depends on the parameters such as the Ra, Da and Ec, determine the fusion temperature corresponding to the maximum heat transfer rate.

Finally, Fig. 11 represents the relation between the total heat transfer and the Darcy number for the various values of porosity. Generally, the total heat transfer increases with increasing Darcy number and porosity. Also, the higher the amount of porosity, the higher the dependency of the Q_t to the Da.

Conclusions

The influence of the nano-encapsulated phase change materials (NEPCM) on the natural convection in a porous annulus has been explored, and the primary outcomes can be summarized as below:

- Using NEPCMs in porous media has improved the heat transfer rate since improving the thermal properties of the base fluid, such as thermal conductivity and heat capacity.
- The critical factor in the enhancement of heat transfer is the dimensionless temperature of fusion (θ_f). As (θ_f) equal to the temperature of cold or hot walls, the heat transfer rate is minimal. Deviation of the fusion temperature (θ_f) from wall temperatures augments the heat transfer rate. The optimum value of the fusion temperature (θ_f) for the highest heat transfer depends on the other parameters such as Ra, Ec and Da.
- Increasing Darcy number (Da) and porosity (ε) lead to a convection heat transfer dominant regime and improve the total heat transfer rate.
- The eccentricity of the hot inner circular cylinder provides a significant influence on the strength of flow circulation and heat transfer. The outcome displays that the highest average Nusselt number is observed when the inner cylinder is positioned at the bottom portion of the domain.
- Radius ratio (Rr) parameter is essential for the control of the heat transfer rate in annulus porous NEPCMs.

References

1. Sajid MU, Ali HM. Thermal conductivity of hybrid nanofluids: a critical review. Int J Heat Mass Transf. 2018;126:211–34.
2. Mahian O, Kolsi L, Amani M, Estellé P, Ahmadi G, Kleinstreuer C, et al. Recent advances in modeling and simulation of nanofluid flows-part I: fundamental and theory. Phys Rep. 2019;790:1–48. https://doi.org/10.1016/j.physrep.2018.11.004
3. Mahian O, Kolsi L, Amani M, Estellé P, Ahmadi G, Kleinstreuer C, et al. Recent advances in modeling and simulation of nanofluid flows-part II: applications. Phys Rep. 2019;791:1–59. https://doi.org/10.1016/j.physrep.2018.11.003
4. Khanafer K, Vafai K, Lightstone M. Buoyancy-driven heat transfer enhancement in a two-dimensional enclosure utilizing nanofluids. Int J Heat Mass Transf. 2003;46(19):3639–53.
5. Jou R-Y, Tzeng S-C. Numerical research of nature convective heat transfer enhancement filled with nanofluids in rectangular enclosures. Int Commun Heat Mass Transfer. 2006;33(6):727–36.
6. Sheikholeslami M, Gorji-Bandpy M, Ganji D, Soleimani S, Seyyedi S. Natural convection of nanofluids in an enclosure between a circular and a sinusoidal cylinder in the presence of magnetic field. Int Commun Heat Mass Transfer. 2012;39(9):1435–43.
7. Ali FH. Numerical simulation of natural convection in an oblique enclosure filled with silver–water nanofluid. Al-Qadisiya J Eng Sci. 2016;9(1):87–105.
8. Wang L, Yang X, Huang C, Chai Z, Shi B. Hybrid lattice Boltzmann-TVD simulation of natural convection of nanofluids in a partially heated square cavity using Buongiorno's model. Appl Therm Eng. 2019;146:318–27.
9. Bhattacharya A, Calmidi VV, Mahajan RL. Thermophysical properties of high porosity metal foams. Int J Heat Mass Transf. 2002;45(5):1017–31.
10. Khan MMA, Ibrahim NI, Mahbubul I, Ali HM, Saidur R, Al-Sulaiman FA. Evaluation of solar collector designs with integrated latent heat thermal energy storage: a review. Sol Energy. 2018;166:334–50.
11. Qureshi ZA, Ali HM, Khushnood S. Recent advances on thermal conductivity enhancement of phase change materials for energy storage system: a review. Int J Heat Mass Transf. 2018;127:838–56.
12. Wu F, Lu D, Wang G. Numerical analysis of natural convection in a porous cavity with the sinusoidal thermal boundary condition using a thermal nonequilibrium model. Numer Heat Transf Part A: Appl. 2016;69(11):1280–96.
13. Leong J, Lai F. Natural convection in a concentric annulus with a porous sleeve. Int J Heat Mass Transf. 2006;49(17–18):3016–27.
14. Alsabery A, Chamkha A, Hussain S, Saleh H, Hashim I. Heatline visualization of natural convection in a trapezoidal cavity partly filled with nanofluid porous layer and partly with non-Newtonian fluid layer. Adv Powder Technol. 2015;26(4):1230–44.
15. Alsabery A, Saleh H, Hashim I, Siddheshwar P. Transient natural convection heat transfer in nanoliquid-saturated porous oblique cavity using thermal non-equilibrium model. Int J Mech Sci. 2016;114:233–45.
16. Alsabery A, Siddheshwar P, Saleh H, Hashim I. Transient free convective heat transfer in nanoliquid-saturated porous square cavity with a concentric solid insert and sinusoidal boundary condition. Superlattices Microstruct. 2016;100:1006–28.
17. Alsabery A, Chamkha A, Saleh H, Hashim I, Chanane B. Effects of finite wall thickness and sinusoidal heating on convection in nanofluid-saturated local thermal non-equilibrium porous cavity. Physica A. 2017;470:20–38.
18. Sivasankaran S, Alsabery A, Hashim I. Internal heat generation effect on transient natural convection in a nanofluid-saturated local thermal non-equilibrium porous inclined cavity. Physica A. 2018;509:275–93.
19. Alsabery A, Chamkha A, Saleh H, Hashim I. Natural convection flow of a nanofluid in an inclined square enclosure partially filled with a porous medium. Sci Rep. 2017;7(1):2357.
20. Chamkha AJ, Ismael MA. Natural convection in differentially heated partially porous layered cavities filled with a nanofluid. Numer Heat Transf Part A: Appl. 2014;65(11):1089–113.
21. Ismael MA, Chamkha AJ. Conjugate natural convection in a differentially heated composite enclosure filled with a nanofluid. J Porous Media. 2015;18(7):699–716.
22. Du K, Calautit J, Wang Z, Wu Y, Liu H. A review of the applications of phase change materials in cooling, heating and power generation in different temperature ranges. Appl Energy. 2018;220:242–73.
23. Fang G, Li H, Yang F, Liu X, Wu S. Preparation and characterization of nano-encapsulated *n*-tetradecane as phase change material for thermal energy storage. Chem Eng J. 2009;153(1–3):217–21.
24. Qiu X, Li W, Song G, Chu X, Tang G. Fabrication and characterization of microencapsulated *n*-octadecane with different crosslinked methylmethacrylate-based polymer shells. Sol Energy Mater Sol Cells. 2012;98:283–93.
25. Jamekhorshid A, Sadrameli S, Farid M. A review of microencapsulation methods of phase change materials (PCMs) as a thermal energy storage (TES) medium. Renew Sustain Energy Rev. 2014;31:531–42.
26. Su W, Darkwa J, Kokogiannakis G. Review of solid–liquid phase change materials and their encapsulation technologies. Renew Sustain Energy Rev. 2015;48:373–91.
27. Liu C, Rao Z, Zhao J, Huo Y, Li Y. Review on nanoencapsulated phase change materials: preparation, characterization and heat transfer enhancement. Nano Energy. 2015;13:814–26.
28. Wickramaratne C, Dhau JS, Kamal R, Myers P, Goswami D, Stefanakos E. Macro-encapsulation and characterization of chloride based inorganic phase change materials for high temperature thermal energy storage systems. Appl Energy. 2018;221:587–96.
29. Barlak S, Sara ON, Karaipekli A, Yapıcı S. Thermal conductivity and viscosity of nanofluids having nanoencapsulated phase change material. Nanoscale Microscale Thermophys Eng. 2016;20(2):85–96.
30. Zhu Y, Qin Y, Wei C, Liang S, Luo X, Wang J, et al. Nanoencapsulated phase change materials with polymer-SiO2 hybrid shell materials: compositions, morphologies, and properties. Energy Convers Manag. 2018;164:83–92.
31. Ghalambaz M, Chamkha AJ, Wen D. Natural convective flow and heat transfer of Nano-Encapsulated Phase Change Materials (NEPCMs) in a cavity. Int J Heat Mass Transf. 2019;138:738–49.
32. Ghalambaz M, Groşan T, Pop I. Mixed convection boundary layer flow and heat transfer over a vertical plate embedded in a porous medium filled with a suspension of nano-encapsulated phase change materials. J Mol Liq. 2019;293:111432.
33. Hajjar A, Mehryan S, Ghalambaz M. Time periodic natural convection heat transfer in a nano-encapsulated phase-change suspension. Int J Mech Sci. 2020;166:105243.
34. Ghalambaz M, Mehryan S, Hajjar A, Veisimoradi A. Unsteady natural convection flow of a suspension comprising Nano-Encapsulated Phase Change Materials (NEPCMs) in a porous medium. Adv Powder Technol. 2019. https://doi.org/10.1016/j.apt.2019.12.010.
35. Oztop HF, Abu-Nada E. Numerical study of natural convection in partially heated rectangular enclosures filled with nanofluids. Int J Heat Fluid Flow. 2008;29(5):1326–36.

36. Varol Y, Oztop HF, Pop I. Entropy analysis due to conjugate-buoyant flow in a right-angle trapezoidal enclosure filled with a porous medium bounded by a solid vertical wall. Int J Therm Sci. 2009;48(6):1161–75.
37. Astanina MS, Sheremet MA, Oztop HF, Abu-Hamdeh N. MHD natural convection and entropy generation of ferrofluid in an open trapezoidal cavity partially filled with a porous medium. Int J Mech Sci. 2018;136:493–502.
38. Arshad A, Ali HM, Ali M, Manzoor S. Thermal performance of phase change material (PCM) based pin-finned heat sinks for electronics devices: effect of pin thickness and PCM volume fraction. Appl Therm Eng. 2017;112:143–55.
39. Ali HM, Ashraf MJ, Giovannelli A, Irfan M, Irshad TB, Hamid HM, et al. Thermal management of electronics: an experimental analysis of triangular, rectangular and circular pin-fin heat sinks for various PCMs. Int J Heat Mass Transf. 2018;123:272–84.
40. Ali HM, Arshad A, Jabbal M, Verdin PG. Thermal management of electronics devices with PCMs filled pin-fin heat sinks: a comparison. Int J Heat Mass Transf. 2018;117:1199–204.
41. Ali HM, Saieed A, Pao W, Ali M. Copper foam/PCMs based heat sinks: an experimental study for electronic cooling systems. Int J Heat Mass Transf. 2018;127:381–93.
42. Shah TR, Ali HM. Applications of hybrid nanofluids in solar energy, practical limitations and challenges: a critical review. Sol Energy. 2019;183:173–203.
43. Abbas N, Awan MB, Amer M, Ammar SM, Sajjad U, Ali HM, et al. Applications of nanofluids in photovoltaic thermal systems: a review of recent advances. Physica A: Stat Mech Appl. 2019;536:122513.
44. Hassan A, Wahab A, Qasim MA, Janjua MM, Ali MA, Ali HM, et al. Thermal management and uniform temperature regulation of photovoltaic modules using hybrid phase change materials-nanofluids system. Renew Energy. 2020;145:282–93.
45. Chai L, Shaukat R, Wang L, Wang HS. A review on heat transfer and hydrodynamic characteristics of nano/microencapsulated phase change slurry (N/MPCS) in mini/microchannel heat sinks. Appl Therm Eng. 2018;135:334–49.
46. Chen B, Wang X, Zeng R, Zhang Y, Wang X, Niu J, et al. An experimental study of convective heat transfer with microencapsulated phase change material suspension: laminar flow in a circular tube under constant heat flux. Exp Therm Fluid Sci. 2008;32(8):1638–46.
47. Khanafer K, Vafai K. A critical synthesis of thermophysical characteristics of nanofluids. Int J Heat Mass Transf. 2011;54(19–20):4410–28.
48. Seyf HR, Zhou Z, Ma H, Zhang Y. Three dimensional numerical study of heat-transfer enhancement by nano-encapsulated phase change material slurry in microtube heat sinks with tangential impingement. Int J Heat Mass Transf. 2013;56(1–2):561–73.
49. Buongiorno J, Venerus DC, Prabhat N, McKrell T, Townsend J, Christianson R, et al. A benchmark study on the thermal conductivity of nanofluids. J Appl Phys. 2009;106(9):094312.
50. Venerus DC, Buongiorno J, Christianson R, Townsend J, Bang IC, Chen G, et al. Viscosity measurements on colloidal dispersions (nanofluids) for heat transfer applications. Appl Rheol. 2010;20(4):11–7.
51. Zaraki A, Ghalambaz M, Chamkha AJ, Ghalambaz M, De Rossi D. Theoretical analysis of natural convection boundary layer heat and mass transfer of nanofluids: effects of size, shape and type of nanoparticles, type of base fluid and working temperature. Adv Powder Technol. 2015;26(3):935–46.
52. Ghalambaz M, Doostani A, Chamkha AJ, Ismael MA. Melting of nanoparticles-enhanced phase-change materials in an enclosure: effect of hybrid nanoparticles. Int J Mech Sci. 2017;134:85–97.
53. Ghalambaz M, Doostani A, Izadpanahi E, Chamkha A. Phase-change heat transfer in a cavity heated from below: the effect of utilizing single or hybrid nanoparticles as additives. J Taiwan Inst Chem Eng. 2017;72:104–15.
54. Schenk O, Gärtner K. Solving unsymmetric sparse systems of linear equations with PARDISO. Future Gener Comput Syst. 2004;20(3):475–87.
55. Wriggers P. Nonlinear finite element methods. Berlin: Springer; 2008.
56. Verbosio F, De Coninck A, Kourounis D, Schenk O. Enhancing the scalability of selected inversion factorization algorithms in genomic prediction. J Comput Sci. 2017;22:99–108.
57. Matin MH, Pop I. Natural convection flow and heat transfer in an eccentric annulus filled by Copper nanofluid. Int J Heat Mass Transf. 2013;61:353–64.
58. Nithiarasu P, Seetharamu K, Sundararajan T. Natural convective heat transfer in a fluid saturated variable porosity medium. Int J Heat Mass Transf. 1997;40(16):3955–67.
59. Ghalambaz M, Sheremet MA, Pop I. Free convection in a parallelogrammic porous cavity filled with a nanofluid using Tiwari and Das' nanofluid model. PLoS ONE. 2015;10(5):e0126486.